SOFC Modeling Considering Electrochemical Reactions at the Active Three Phase Boundaries

Andersson, Martin; Yuan, Jinliang; Sundén, Bengt

Published in:
International Journal of Heat and Mass Transfer

DOI:
10.1016/j.ijheatmasstransfer.2011.10.032

2012

SOFC Modeling Considering Electrochemical Reactions at the Active Three Phase Boundaries

Martin Andersson, martin.andersson@energy.lth.se
Jinliang Yuan, jinliang.yuan@energy.lth.se
Bengt Sundén, bengt.sunden@energy.lth.se

Department of Energy Sciences,
Lund University, P.O. Box 118
SE-221 00, Lund, Sweden.

Corresponding author:
Martin Andersson
martin.andersson@energy.lth.se
+46 46 222 49 08 (phone)
+46 46 222 47 17 (fax)

ABSTRACT

It is expected that fuel cells will play a significant role in a future sustainable energy system, due to their high energy efficiency and the possibility to use renewable fuels. A fully coupled CFD model (COMSOL Multiphysics) is developed to describe an intermediate temperature SOFC single cell, including governing equations for heat, mass, momentum and charge transport as well as kinetics considering the internal reforming and the electrochemical reactions. The influences of the ion and electron transport resistance within the electrodes, as well as the impact of the operating temperature and the cooling effect by the surplus of air flow, are investigated. As revealed for the standard case in this study, 90 % of the electrochemical reactions occur within 2.4 μm in the cathode and 6.2 μm in the anode away from the electrode/electrolyte interface. In spite of the thin electrochemical active zone, the difference to earlier models with the reactions defined at the electrode-electrolyte interfaces is significant. It is also found that 60 % of the polarizations occur in the anode, 10 % in the electrolyte and 30 % in the cathode. It is predicted that the cell current density increases if the ionic transfer tortuosity in the electrodes is decreased, the air flow rate is decreased or the cell operating temperature is increased.

Keywords: SOFC, CFD modeling, charge transport, electrochemical reactions, TPB

1. INTRODUCTION

Fuel cells (FCs) are promising due to the advantages of higher efficiency and lower emissions of SO_X, NO_X and CO_2, compared to conventional power generation devices. Solid oxide fuel cells (SOFCs) are generally more tolerant to contaminants than other fuel cells and the possibility to internally (as well as externally) reform the hydrocarbon fuels make them interesting for renewable energy resources [1]. Validated models are necessary to understand various transport processes and reactions for improving the cell performance. However, a validity range should be evaluated between the developed models and experimental data. It should be noted that CFD (computational fluid dynamics) models make it possible to reduce the amount of experimental tests needed for cell development, and only a limited amount of tests is then required to validate the accuracy of the models [2-3], as revealed in recent reviews on solid oxide fuel cell modeling and development by Wang *et al.* [4], Kakac *et al.* [5] and Andersson *et al.* [6].

The focus and the selected scale (system, stack, cell, component or functional materials) differ significantly between different models, as described in the open literature. For example, two approaches for defining the electrochemical reactions can be found in the literature, either as source terms in the governing equations [7] or as interface conditions defined at the electrode/electrolyte interfaces [8-9]. When the interface condition approach is applied the ionic resistance in the electrodes is neglected and the electrochemical reactions reduce to the interface conditions in the governing equations for heat, mass and momentum transport.

Shi *et al.* [10] developed a 2D CFD model, including phenomena of heat, mass, ion, and electron transport as well as electrochemical reactions. Heterogeneous electrode properties were also taken into account by linear functionally graded porosity and various nonlinear distributions according to their cell design. Also Ni *et al.* [11] studied heterogeneous electrodes, but at the microscale level, and their model predicts the overpotential losses by capturing the coupled mass transfer and the electrochemical reactions. A 2D isothermal mechanistic model for a SOFC button cell was developed by Shi *et al.* [12], including polarization effects, molecular and Knudsen diffusion, gas transport, ionic and electronic conduction, surface diffusion of intermediate species and electrochemical reactions. Kanno *et al.* [13] and Iwai *et al.* [14] introduced a concept of different tortuosity factors for the transport of ions, electrons and gas-phase molecules, i.e., the real (average) transport distance for the ions and the electrons within the electrodes was evaluated and applied in the simulation. The tortuosity factors can be calculated, for example, by the lattice Boltzmann method.

An early polarization model, involving the Butler-Volmer equation, was developed by Chan *et al.* [15] in 2001 to lift the limitations of the Tafel equation. Patcharavorachot *et al.* [16] developed a pure electrochemical reaction model, i.e., neglecting the mass and the heat transport, the fluid flow and the internal reforming reactions. Bessler *et al.* [17] studied electrochemistry of SOFC anodes, focusing on the nickel/yttria-stabilized zirconia (Ni/YSZ) materials, and the electrochemical reactions were described in multi-steps in the Arrhenius form. The Butler-Volmer equations are often used to describe the overpotential/current density relationship, however, a more detailed approach was developed by Bessler *et al.* [18] to include an elementary-kinetic multistep description of electrochemistry with coupled surface chemistry, charge-transfer reactions, physical representation of the electric potential steps and other transport phenomena. On the other hand, in the above mentioned models, only pure hydrogen is considered for the electrochemical reactions at the fuel side, i.e., it is

assumed that carbon monoxide and methane are fully reformed to hydrogen before the electrochemical reactions occur. This limitation was released by Hajimolana *et al.* [19].

SOFCs enable internal reforming of hydrocarbons with relatively short carbon chains. A review on the reaction kinetics was given by Mogensen *et al.* in [20] and it is concluded that there are large differences in the published kinetic expressions for the steam reforming reactions. Vakouftsi *et al.* [21] developed a 3D CFD model for a planar SOFC, including mass transport, electrochemical reactions and global scale kinetic expressions for the methane steam reforming reaction (MSR) and the water-gas shift reaction (WGSR) in the Arrhenius form. Nagel *et al.* [22] studied the relations between mass, heat and charge transport within SOFCs, using a finite volume method, considering different fuel gas compositions. A dynamic SOFC model, including mass and energy balances, electrochemical reactions and internal reforming reaction kinetics, was developed by Aguiar *et al.* [23] to study load step-changes. A heterogeneous chemistry multistep mechanism for the steam reforming reaction of methane and carbon monoxide in the SOFC anode was presented by Janardhanan and Deutschmann in [24], including 21 reversible reaction steps for 6 gas-phase species and 12 surface-adsorbed species.

The aim of this work is to investigate the influence of the ion and electron transport resistance within the anode and cathode by solving a fully coupled CFD model including the governing equations for heat, mass, momentum, ion and electron transport occurring in an intermediate temperature SOFC single cell. The advances compared to our previous work [3,6,8] include the addition of the governing equations for the ion transport (in YSZ) and the electron transport (in Ni or LSM), i.e., the current density distributions are calculated from local conditions (2D) throughout the cell, instead of just defining an average value (0D) [3,25] or with a 1D approach at the electrode/electrolyte interface [7]. Further advances are made for the electrochemical reactions, which are defined as source terms instead of interface conditions (as in [3,7,25]) concerning mass, heat, momentum, ion and electron governing transport equations. The uniqueness of this paper by the macroscale approach, is the implementation of the tortuosity factors and the material specific volume fractions for the ion and electron transport within the electrodes, combined with a complete set of simultaneously solved governing equations with the global internal reforming reaction kinetics. Other operating parameters are kept constant, while the inlet temperature, the air flow rate or the ionic tortuosity are varied for conducting a parameter study.

2. MATHEMATICAL MODEL AND MAJOR ASSUMPTIONS

A 2D CFD model for an anode-supported SOFC is developed and implemented in the commercial software, COMSOL Multiphysics (version 4.1). The equations for momentum, mass, ion, electron and heat transport are solved simultaneously. The geometry, based on a standard cell (Figure 1) by Ningbo Institute of Material Technology and Engineering (NIMTE), China, is defined in Table I, and a sketch of the investigated cell can be seen in Figure 2. Note that Figure 2 is not to scale.

The NIMTE standard cell consists of a 400 μm thick Ni (40 %)/YSZ (60 %) anode substrate and additionally an active anodic layer of 15 μm, where the electrochemical reactions occur. The electrolyte is a 10 μm thick layer of YSZ. The cathode consists of a 20 μm thick active layer of LSM/YSZ and a buffer layer of 50 μm LSM. Note that the anode active- and support layers have the same material composition, and the interface may not be very distinct, compared to the cathode, where the active and support layers have different compositions. It is a fact

that a fine porous microstructure with a high surface area may lead to a decreased mechanical strength. Because the TPB does not extend too far from the anode–electrolyte interface, a graded porosity can be used to maximize the length of the TPBs in the active region. The high mechanical strength is maintained for the rest of the anode which is used primarily as the cell support and for the internal reforming reactions, when hydrocarbons are supplied as the fuels.

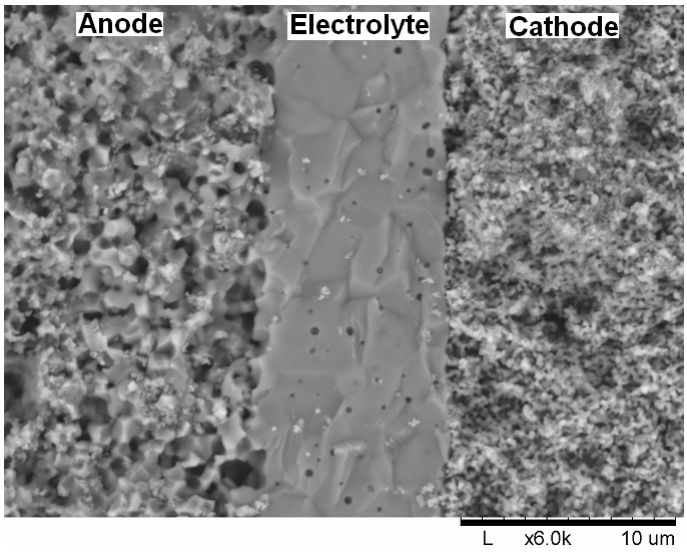

Figure 1. A SEM image of a tested SOFC cross-section, with (from left to right) anode active layer, electrolyte and cathode active layer.

TABLE I. CELL GEOMETRY

Cell Component	Thickness
Cell length	0.1 m
Fuel channel height	1 mm
Air channel height	1 mm
Anode thickness	415 μm
Cathode thickness	70 μm
Electrolyte thickness	10 μm
Interconnect thickness	300 μm

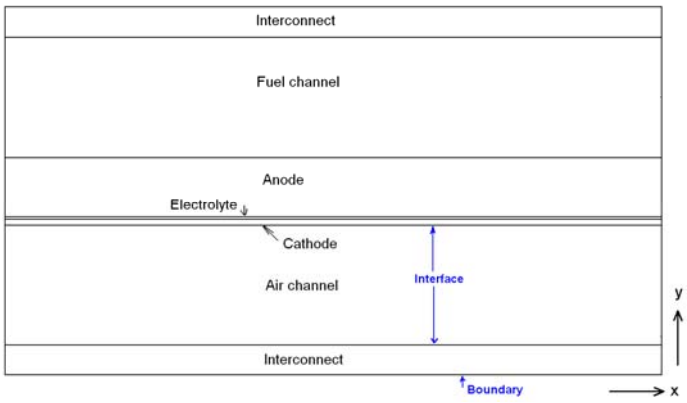

Figure 2. Sketch of an anode-supported SOFC (not to scale).

2.1. *Heat transport*

A local temperature equilibrium (LTE) approach is applied, i.e., the temperature is assumed to be locally the same for the gas- and solid-phases (within the electrodes). Previously a local temperature non-equilibrium (LTNE) approach have been applied [3]. However, the temperature difference between the solid- and gas-phases within the electrodes is found to be neglible. The governing equation for the temperature distribution is in this work defined as:

$$\rho_g \cdot c_{p,g} \cdot \vec{\mathrm{u}} \cdot \nabla T = \nabla \bullet \left(k_{eff} \nabla T\right) + Q_h \tag{1}$$

where Q_h is the heat generation/consumption (source term defined in eqns (8)-(11)), T the temperature, k_{eff} the effective thermal conductivity, c_p the gas-phase specific heat, ρ_g the gas-phase density and $\vec{\mathrm{u}}$ the velocity vector. The overall governing equation for the heat transport, eqn (1), reduces to pure heat conduction in the electrolyte and the interconnector. The effective value of the thermal conductivity in the porous electrodes can be specified as [7]:

$$k_{eff} = \varepsilon \cdot k_g + (1-\varepsilon) \cdot k_s \tag{2}$$

where ε is the porosity, *eff* means effective, *s* solid and *g* gas-phase. The conductivity, the specific heat and the density for the solid materials in the different subdomains are outlined in Table II.

TABLE II. MATERIAL PARAMETERS

	Thermal conductivity [5] (W/m/K)	**Specific heat [24]** (J/kg/K)	**Density [24]** (kg/m^3)
Anode (Ni/YSZ)	11	450	3310
Cathode (LSM/YSZ)	6	430	3030
Electrolyte (YSZ)	2.7	470	5160
Interconnect (stainless steel)	20	550	3030

The specific heat for each gas species and the gas mixture is calculated as [26]:

$$c_{p,i} = \sum_{k=1}^{7} \mathrm{a_k} \cdot \left(\frac{T}{1000}\right)^k \tag{3}$$

$$c_{p,g} = \sum_i x_i \cdot c_{p,i} \tag{4}$$

where $\mathrm{a_k}$ is the species dependent parameter (extracted from [26]) and "k" stands for the number of parameters involved in the specific heat calculation. The thermal conductivity for each species of the gas-phase, as well as for the gas mixture, is defined as [26]:

$$k_i = 0.01 \cdot \sum_{k=1}^{7} c_k \cdot \left(\frac{T}{1000}\right)^k \tag{5}$$

$$k_g = \sum_i x_i \cdot k_i \tag{6}$$

where c_k is the species dependent parameter (extracted from [26]) and "k" stands for the number of parameters in the thermal conductivity evaluation.

The heat consumption/generation due to the internal reforming reactions in the anode is implemented by:

$$Q_{h,ref} = r_{ref} \cdot \Delta H_{ref} \tag{7}$$

where r_{ref} is the reaction rate (in mol/m^{3}s) and ΔH_{ref} the enthalpy change of the reforming reactions. The reaction rate will be introduced in section 2.6. The heat generation due to the activation and the concentration polarizations is defined as [19,25]:

$$Q_{h,act+conc} = -\left(\eta_{act,e} + \eta_{conc,e}\right) \cdot i \cdot AV_e \tag{8}$$

where i is the ion current density, η_{act} the activation polarization (defined in section 2.4), η_{conc} the concentration polarization (defined in section 2.4), AV_e the electrochemical active area to volume ratio. The AV_e is for the anode and the cathode are calculated by comparing the model versus experimental data as described in section 3. The heat generation due to the ohmic polarization is calculated as [19,25]:

$$Q_{h,ohm} = \frac{i_s^2}{\sigma_s} + \frac{i_l^2}{\sigma_l} \tag{9}$$

where σ is the conductivity, i the current density, l the index for the electrolyte material (YSZ) and s for the electrode materials (Ni or LSM). This is an extension and improvement compared to our previous models [3,8,25], where the ion transport in the YSZ within the anode and the cathode is neglected. The expressions for ionic and electronic conductivity are introduced in section 2.4.

The amount of the heat generated (within the cathode side)/consumed (within the anode side) due to the change of entropy in the electrochemical reactions is defined as [25]:

$$Q_{h,e} = -\Delta S_e \frac{T \cdot i \cdot AV_e}{n_e \cdot \mathrm{F}} \tag{10}$$

where F is the Faraday constant, n_e the number of electrons transferred per reaction and ΔS_e the entropy change of the electrochemical reactions, calculated from the data in [27] for the anode and the cathode TPBs, respectively. The inlet gas temperature is defined by the operating temperature (1010 K) and the outlet is defined as a

convective flux. The boundaries at the top and the bottom of the cell are defined as symmetry conditions, because it is assumed that the cell is surrounded by other ones with the identical temperature distribution.

2.2. Mass transport

In the porous material, there are two kinds of mass diffusion mechanisms: molecular and Knudsen diffusions. The molecular diffusion (collisions between gas molecules) is significant in the case of large pores, whose size is much bigger than the mean free path of the diffusion gas molecules [12,28]. The Knudsen diffusion is important when the mean free path is of the same order or bigger than the pore size, and the molecules collide with the solid walls more often than with other molecules**.** At the SOFC operating temperature, the mean free path of these gas components is about 0.2-0.5 μm. In this study, the radius of pores is assumed as 0.34 μm, which is of the same order as the mean free path, i.e., the Knudsen diffusion should be included in the SOFC models. The Knudsen diffusion coefficient of the gas component *i* with the component *j* in a gas mixture, $D_{k,ij}$, is calculated based on the free molecule flow theory, [7]:

$$D_{K,ij} = \frac{2}{3} \cdot r_e \cdot \sqrt{\frac{8 \cdot \mathrm{R} \cdot T}{\pi \cdot M_{ij}}} \tag{11}$$

$$M_{ij} = \frac{2}{\frac{1}{M_i} + \frac{1}{M_j}} \tag{12}$$

where r_e is the effective radius of the pores and R the universal gas constant.

The ordinary diffusion coefficients (D_{ij}), for a multi-component gas mixture system, are calculated as [29]:

$$D_{ij} = \frac{2.66 \cdot 10^{-8} \cdot T^{3/2}}{p \cdot M_{ij}^{1/2} \cdot l_{ij}^2 \cdot \Omega_D} \tag{13}$$

where l_{ij} is the characteristic length and Ω_D the diffusion collision integral, as defined in [29]. In the porous media, there is a reduced void volume and an increased diffusion length based on the local microstructures, and the coefficients are usually corrected by porosity and tortuosity, respectively [7,28]:

$$D_{eff,ij} = \frac{\varepsilon}{\tau} \cdot r_e \cdot \left(\frac{D_{ij} \cdot D_{K,ij}}{D_{ij} + D_{K,ij}} \right) \tag{14}$$

Equation (15) is used to describe the mass transport phenomena for each gas component inside the cell and solved for the fuel- and air channels and the electrodes.

$$-\nabla\left(\rho \cdot w_i \sum^{n} D_{eff,ij} \cdot \nabla x_j \right) + \left(\left(x_j - w_j \right) \frac{\nabla p}{p} \cdot \left(\nabla \bullet \vec{\mathrm{u}} \right) \right) - \nabla\left(D_i^T \cdot \frac{\nabla T}{T} \right) + \rho \cdot \vec{\mathrm{u}} \cdot \nabla w_j = S_i \tag{15}$$

where w is the mass fraction, x the mole fraction, n the number of species and D_i^T the thermal diffusion coefficient. S_i, the source term by the chemical reactions, is defined for the internal reforming (within the anode) and the electrochemical reactions (within the anode and cathode). The fuel inlet conditions (mole fractions) are defined as 30 % pre-reformed natural gas, as defined by International Energy Agency (IEA): $x_{H2} : x_{CH4} : x_{CO} : x_{H2O} : x_{CO2} = 0.2626 : 0.171 : 0.0294 : 0.4934 : 0.0436$ [22]. The air inlet is defined as air, including oxygen and nitrogen. The fuel and gas channel outlets are defined as convective fluxes.

2.3. Momentum transport

The Darcy-Brinkman equation, eqn (16), is introduced and solved for the gas flow in the fuel and air channels, and in the porous materials simultaneously [3]:

$$\left(\frac{\mu}{\kappa}+\rho\cdot\nabla\bullet\vec{u}\right)\cdot\vec{u}-\nabla\left[-p+\frac{1}{\varepsilon}\left\{\Psi-\left(\frac{-2}{3}\cdot\mu\right)(\nabla\bullet\vec{u})\right\}\right]=\mathbf{F} \tag{16}$$

where **F** is the volume force vector, κ the permeability of the porous medium ($1.76\cdot10^{-11}$ m^2 [5]), ε_p the porosity, μ the dynamic viscosity and Ψ the viscous stress tensor. The densities for the participating gases are calculated, according to the ideal gas law [30]:

$$\rho_g=\frac{p\cdot\sum x_i\cdot M_i}{\mathrm{R}\cdot T} \tag{17}$$

The dynamic viscosity for each participating species in the gas-phase, as well as for the gas mixture, is evaluated as [26]:

$$\mu_i=\sum_{k=1}^{7}\mathrm{b_k}\cdot\left(\frac{T}{1000}\right)^k \tag{18}$$

$$\mu_g=\sum_i x_i\cdot\mu_i \tag{19}$$

where b_k is the species dependent parameter and "k" stands for the number of species dependent parameters in the viscosity equation.

The gas inlets velocities are defined as a laminar flow profile, and the average values are based on the fuel- and oxygen utilization, i.e., 70 % and 18 %, respectively, for the standard case in this study. At the outlets the pressure (1 atm) is fixed.

2.4. Ion and electron transport

The potential difference between the anode and the cathode current collectors corresponds to the total cell voltage. The governing equations for the ion and electron transport are implemented as:

$$i_l = -\sigma_l \nabla \phi_l \tag{20}$$

$$i_s = -\sigma_s \nabla \phi_s \tag{21}$$

where ϕ is the potential. The potential at the anode current collector is set to zero and the potential at the cathode current collector is set as the cell operating voltage (0.7 V in this study). All other boundaries and interfaces are electrically insulated. The electronic conductivities in the anode ($\sigma_{s,a}$) and the cathode ($\sigma_{s,c}$), and the ionic conductivity in the electrolyte material ($\sigma_{l,el}$) are calculated as [16,19,31]:

$$\sigma_{s,a} = \frac{4.2 \cdot 10^7}{T} \cdot \exp\left(\frac{-1200}{T}\right) \tag{22}$$

$$\sigma_{l,el} = 33.4 \cdot 10^3 \cdot \exp\left(\frac{-10300}{T}\right) \tag{23}$$

$$\sigma_{s,c} = \frac{9.5 \cdot 10^7}{T} \cdot \exp\left(\frac{-1150}{T}\right) \tag{24}$$

The actual lengths that the ions and electrons are transported in the electrodes increase due to the real/functional material compositions and their micro structures. This is accounted for by using the structure-dependent tortuosity factors and the volume fractions. The effective ionic- and electronic conductivity in the electrodes are defined as [13]:

$$\sigma_{l,e,YSZ} = \sigma_{l,e} \cdot \frac{V_{YSZ,e}}{\tau_{YSZ,e}} \tag{25}$$

$$\sigma_{s,a,Ni} = \sigma_{s,a} \cdot \frac{V_{Ni,a}}{\tau_{Ni,a}} \tag{26}$$

$$\sigma_{s,c,LSM} = \sigma_{s,c} \cdot \frac{V_{LSM,c}}{\tau_{LSM,c}} \tag{27}$$

where τ is the tortuosity factor and V the volume fraction for the specific materials. Note that the ionic conductivity in the electrodes was not included in our previous work [3,6,8,25]. To the authors knowledge this is the first cell scale SOFC model, which considers the microstructure effects by including the tortuosity factors and material volume fractions for the ion and electron transport within the anode and the cathode. As found later in this work, the influence is significant on both the ion transport from the electrolyte to the active TPB areas and the ohmic polarization. Kanno *et al*. calculated (by LBM) the tortuosity factors and the values between 7 and 17 are found for Ni and between 6 and 14 for YSZ, respectively [13]. Iwai *et al*. evaluated the tortuosity factors statistically with the random walk process of nonsorbing particles as well as with the LBM method, and values between 6.91 and 29.46 were found for Ni and between 9.84 and 27.89 for YSZ, respectively, depending slightly on the evaluation methods, but mostly on the direction (x, y and z) [14]. Vivet *et al.* [32] calculated the

tortuosity in the range of 3.04 and 6.24 for Ni, and between 1.79 and 2.10 for YSZ, respectively. For this work the dimensionless parameters for the electrode structure stated in Table III are employed. It is worthwhile to note that there is an negligible transport of oxygen ions in Ni material and of electrons in YSZ material [32], and therefore it is not considered in this study.

TABLE III. CHARGE TRANSPORT PORPERTIES FOR THE POROUS ELECTRODES

	V_{YSZ}	V_{Ni} or V_{LSM}	ε_e	τ_s	τ_l
Anode	0.42	0.28	0.30	10	10
Cathode	0.42	0.28	0.30	10	10

The activation polarizations (η_{act}) are defined as [30]:

$$\eta_{act,a} = \phi_s - \phi_l - E_{eq,a} \tag{28}$$

$$\eta_{act,c} = \phi_s - \phi_l - E_{eq,c} \tag{29}$$

where the index *a* stands for the anode, *c* for the cathode, and E_{eq} is the equilibrium voltage.

The electromotive force (ideal voltage after partial pressure consideration, E^{OCV}) is determined by the difference in thermodynamic potentials of the electrode reactions [16, 33]. Due to the internal resistance and the polarizations, the actual voltage (E) becomes less than the ideal voltage, and is expressed as [16]:

$$E = E^{OCV} - \eta_{act} - \eta_{ohm} - \eta_{conc} \tag{30}$$

The concentration polarizations (η_{conc}) are calculated by [3,34]:

$$\eta_{conc,a} = \frac{\mathrm{R} \cdot T}{n_{e,a} \cdot \mathrm{F}} \cdot \ln\left(\frac{p_{H_2O,TPB} \cdot p_{H_2,b}}{p_{H_2,TPB} \cdot p_{H_2O,b}} \right) \tag{31}$$

$$\eta_{conc,c} = \frac{\mathrm{R} \cdot T}{n_{e,c} \cdot \mathrm{F}} \cdot \ln\left(\frac{p_{O_2,b}}{p_{O_2,TPB}} \right) \tag{32}$$

where the index *TPB* stands for the three phase boundary (TPB) and *b* for the boundary between the gas channel and the electrode.

When a hydrogen-steam mixture is used as fuel, the electromotive force can be calculated by the standard Nernst equation [16]:

$$E^{OCV}_{H_2/O_2} = E^{0}_{H_2/O_2} - \frac{\mathrm{R} \cdot T}{2 \cdot \mathrm{F}} \cdot \ln\left(\frac{p_{H_2O}}{p_{H_2} \sqrt{p_{O_2}}} \right) \tag{33}$$

$$E^0_{H_2/O_2} = 1.253 - 2.4516 \cdot 10^{-4} \cdot T \tag{34}$$

where E^0 is the ideal voltage before partial pressure consideration and p_i the partial pressure, at the TPB, in atm. It should be noted that eqns (33)-(34) are only valid for pure hydrogen-steam mixtures. The electromotive force for only carbon monoxide or methane as fuel is presented in eqns (35)-(36), respectively. E^0 for carbon monoxide decreases with increased temperature, but it is not temperature dependent for methane, due to a constant molar number of the products and the reactants [33,35]. In this study only eqns (33)-(34) are used to calculate the electromotive force, i.e., it is assumed that methane and carbon monoxide fully react with steam and only H_2 participates in the electrochemical reactions. For the case of pre-reformed natural gas ($H_2/H_2O/CH_4/CO/CO_2$) present, the Nernst equation may not be the most applicable expression. Our aim is to release this limitation in our future studies.

$$E^{OCV}_{CO/O_2} = E^0_{CO/O_2} - \frac{\mathrm{R} \cdot T}{2 \cdot \mathrm{F}} \cdot \ln\left(\frac{p_{CO_2}}{p_{CO}\sqrt{p_{O_2}}} \right) \tag{35}$$

$$E^{OCV}_{CH_4/O_2} = E^0_{CH_4/O_2} - \frac{\mathrm{R} \cdot T}{8 \cdot \mathrm{F}} \cdot \ln\left(\frac{p_{CO_2} \cdot {p_{H_2O}}^2}{p_{CH_4} \cdot {p_{O_2}}^2} \right) \tag{36}$$

2.5. Electrochemical reactions

The cathodic electrochemical reactions within an SOFC can be described globally as: oxygen is reduced at the cathodic TPB, eqn (37). The oxygen ions are transported through the YSZ (in the electrodes and electrolyte), and the electrons are prevented to pass through the electrolyte. The anodic electrochemical reactions between hydrogen and oxygen ions, eqn (38), take place at the anodic TPB [11,24].

$$\frac{1}{2}O_2 + 2e^- \Leftrightarrow O^{2-} \tag{37}$$

$$H_2 + O^{2-} \Leftrightarrow H_2O + 2e^- \tag{38}$$

The current density (per unit volume) in the anode as well as in the cathode is calculated, by the Butler-Volmer equation [15]:

$$i_e = AV_e \cdot i_{0,e} \left\{ \exp\left(\beta \cdot \frac{n_e \cdot \mathrm{F} \cdot \eta_{act,e}}{\mathrm{R} \cdot T} \right) - \exp\left(-(1-\beta) \frac{n_e \cdot \mathrm{F} \cdot \eta_{act,e}}{\mathrm{R} \cdot T} \right) \right\} \tag{39}$$

where β is the transfer coefficient, usually assumed to be 0.5. The Butler-Volmer equation can then be expressed as [15]:

$$i_e = AV_e \cdot 2 \cdot i_{0,e} \cdot \sinh\left(\frac{n_e \cdot \mathrm{F} \cdot \eta_{act,e}}{2 \cdot \mathrm{R} \cdot T} \right) \tag{40}$$

where $i_{0,e}$ is the exchange current density. The exchange current density is calculated by [16,23]:

$$i_{0,e} = \frac{R \cdot T}{n_e \cdot F} A_{i,e} \cdot \exp\left(\frac{-E_{a,e}}{\mathrm{R} \cdot T}\right) \tag{41}$$

where the pre-exponential factor ($A_{i,e}$) is $2.35 \cdot 10^{11}$ $\Omega^{-1}m^{-2}$ for the cathode and $6.54 \cdot 10^{11}$ $\Omega^{-1}m^{-2}$ for the anode, respectively. An activation energy ($E_{a,e}$) of 137 kJ/mol for the cathode and 140 kJ/mol for the anode are used by Patcharavorachot *et al.* [16] and Aguiar *et al.* [23], while the values between 110 and 140 kJ/mol for the anode and 130 and 190 kJ/mol for the cathode appear in various work available in the open literature [5,36-40].

The influence of different polarizations/potentials varies depending on cell structure/design and operating conditions. The different potentials vary along the flow direction and they are affected by, for example, the local temperature as well as the local hydrogen and oxygen concentrations. It is concluded in Sohn *et al.* [41] that for an intermediate temperature SOFC with a co-flow configuration, the activation polarization is dominant in the cathode near the fuel and air inlets, and in the anode near the outlets. Also the counter-flow configuration was investigated and the variation in the cathodic activation overpotential is smaller, compared to the co-flow configuration. For both the co-flow and the counter-flow configurations the activation polarization in the cathode is dominating at lower current densities and the activation polarization in the anode at higher ones. The dominance of the anode activation at high current densities is explained by the depletion of hydrogen according to a high fuel utilization [41]. The influence from the ionic polarization depends mostly on the ionic transfer conductivity within the electrolyte and the electrolyte thickness, where a decreased thickness means a decreased ohmic polarization. When the concentration of fuel or oxidant reaches zero at the TPB, the concentration overpotentials increase and the voltage reaches zero [23]. Bessler *et al.* [18] studied an electrode-supported SOFC and found that the polarizations within the cathode are small compared to the one within the anode or electrolyte. Xiao *et al.* [42] investigated an anode supported SOFC with a Ni/YSZ anode and a LSM cathode and concluded that the cathodic polarization decreases with increasing temperature, but the anodic polarization increases with increasing temperature, partly due to an increase in the resistivity of the Ni/YSZ cermet connected to the drop in metallic conductivity as the temperature increases.

2.6. Internal reforming reactions

When a fuel containing methane and carbon monoxide is supplied, the reforming reactions take place within the anode. Methane reacts with steam in the MSR (eqn (42)). Carbon monoxide can be oxidized in the electrochemical reaction, but mainly reacts further with water in the WGSR (eqn (43)) [11]. The reaction kinetics from Klein *et al.* [43] for the MSR (an Arrhenius form expression dependent on the active area to volume ratio) and from Haberman and Young [44] for the WGSR are used to calculate the reaction rates in this work. The range for the AV_{MSR} (related to catalytic kinetic reactions) varies in the literature between $1 \cdot 10^5$ m^2/m^3 [45] and $2.2 \cdot 10^6$ m^2/m^3 [43] for SOFC anodes. The AV_{MSR} can be compared to the total measured surface area to volume ratio (AV_{tot}), that reaches $1 \cdot 10^8$ m^2/m^3 for Ni/YSZ material developed for SOFC anodes (with a nickel content of 50 %, surface area of 27 m^2/g and a power density of 3.75 g/cm^3 [46]), while the surface area in Mamak *et al.* [47] reaches 162-112 m^2/g for the materials containing 13-40 mole-% Ni or NiO. Note that not all the surfaces are available for the catalytic reactions, due to the distribution of catalyst, dead pores and mass transfer limitations among others. An AV_{MSR} of $7 \cdot 10^6$ m^2/m^3 is applied in this work, which corresponds to 7

percent of the total Ni/YSZ surface area to volume ratio, when compared to the AV_{tot} in Aruna *et al.* [46]. The relatively high AV_{MSR} compensates partly for a high activation energy in the Klein kinetics.

$$CH_4 + H_2O \Leftrightarrow 3H_2 + CO \quad \text{(MSR)} \tag{42}$$

$$CO + H_2O \Leftrightarrow H_2 + CO_2 \quad \text{(WGSR)} \tag{43}$$

3. SOLUTION METHODS AND MODEL VALIDATION

All the equations, defined in section 2 above, are numerically solved in COMSOL Multiphysics (version 4.1:0.185) using a stationary segregated solver with a direct (MUMPS) linear solver system. The governing equations are segregated in 5 different groups: **1.** velocity field, pressure distribution and pressure corrections, **2.** temperature distribution, **3.** ion and electron distribution, **4.** mass fraction distribution on the air side (O_2/N_2) and **5.** mass fraction distribution on the fuel side ($H_2/H_2O/CH_4/CO/CO_2$). The segregated solver solves for 2 290 000 degrees of freedom and the tolerance is defined to 0.001 for each segregated group. Grid independence was achieved at 716 000 elements, after which the change in the maximum temperature is less than 0.08 %, in the maximum air velocity less than 0.36 %, in the minimum oxygen mole fraction less than 0.25 %, in the minimum hydrogen mole fraction less than 0.35 %, in the methane conversion less than 0.22 % and in the maximum current density at the inlet less than 0.07 % (compared with the predictions by 1 180 000 elements). It should be noted that the mesh is finest close to the electrode/electrolyte interface and coarsest for the air- and fuel channels and for the interconnects. The reason for such a mesh arrangement is mainly due to the charge transport and the electrochemical reactions (affecting the governing transport equations for ion, electron, mass, heat and momentum) appearing only in the regions close to the electrode/electrolyte interface.

Numerical results of any SOFC models are only approximations of real conditions and the validation is an important and necessary step in the development of reliable and accurate computational models. A range of validity should be evaluated and can be established by comparing the developed model with experimental data. It should be noted that CFD models make it possible to reduce the amount of experimental tests needed for cell development. Our model relies on the experimental data from a standard cell developed at Ningbo Institute of Material Technology & Engineering (NIMTE) in China. The air- and fuel flow rates and operating temperature are implemented in the model directly for the validation, and the AV_e for the anode and the cathode is calculated/validated from the voltage/current density measurements. For the experiments a fuel flow rate of 800 sccm (standard cubic centimeters per minute) and an air flow rate of 2000 sccm are used. The single cell sample has dimensions of $5 \cdot 5.8$ cm^2, with an active area of $4 \cdot 4$ cm^2. An alumina testing house is used, where the cell temperature is kept constant during the tests, i.e., 750 °C for this case. Voltage probes are placed on the surface of the anode- and cathode support. The NIMTE standard cell design/structure is defined in section 2 above. Note that the validation performed covers overall phenomena occurring at the macroscale only. An extended validation including transport and reaction phenomena occurring in the microscale is also interesting for future studies.

4. RESULTS AND DISCUSSION

The predicted temperature increases along the x-direction (the main flow direction), as seen in Figure 3. Heat is generated due to the change of entropy by the electrochemical reactions in the cathode, as well as the activation-, ohmic- and concentration polarizations within the anode, electrolyte and cathode, and the WGSR in the anode. On the other hand heat is consumed in the anode, due to change of entropy by the electrochemical reactions and the MSR. The predicted temperature difference in the y-direction inside the air channel occurs because the convective heat flux is bigger compared to the fuel channel due to the relatively larger mass flow rate.

The ion current density along the y-direction (i.e., the cross-section normal to the flow direction) is shown in Figure 4 at the inlet and the outlet. For the standard case the current density distribution shows a similar behavior at the inlet and outlet, because the decrease of ideal voltage due to the temperature increase and the consumption of fuel and oxygen is compensated by an increase of the current density due to an increased cell temperature. It can be seen that the current density gradients are steeper on the cathode side, than on the anode side. In this model the volume fractions of the solid materials and pores as well as the tortuosities are accounted for, as defined in eqns (30)-(32), to better describe realistic transport distances for the ions and the electrons within the anode and the cathode. This means an increased ion/electron resistance, compared to the simplified models. In this study the electrochemical reactions are implemented as source terms in the governing equations for heat, mass, momentum, ion and electron transport. The electrochemical reactions occur within a few micro meters close to the electrode/electrolyte interface, as shown in Figure 4. It is found that the electrochemical reaction zone is only 2.4 μm deep in the active region from the interface in the cathode, and 6.2 μm in the anode. This zone is defined as where the ion current density is higher than 300 A/m², i.e., around 10 % of the maximum value at the inlet for the standard case. The depth of the electrochemically active reaction zones is quite small compared to the designed active layers with a finer structure and a higher surface area than the ones in the buffer layers. As mentioned above, for the NIMTE standard cell, the thickness of the active layers is 20 μm and 15 μm for the cathode and the anode, respectively.

The potential distribution is shown in Figure 5 for the positions close to the inlets and the outlets. The ideal voltage decreases along the flow direction due to both the temperature increase and the consumption of fuel and oxygen. It can be revealed from Figure 5 that around 60 % of the polarizations occur in the anode, 10 % in the electrolyte and 30 % in the cathode, i.e., any efforts to improve the fuel cell performance should be focused on decreasing the anode activation polarization, or improving the volumetric current density on the anode side. These findings are different compared to our previous predictions [3,6,8], where the electrochemical reactions are defined at the electrode/electrolyte interfaces only and the cathodic activation polarization dominates over the anodic one. This difference might be particular due to a larger active TPB AV_e applied on the cathodic side ($2.6 \cdot 10^6$ m^2/m^3) compared to the anode side ($1.3 \cdot 10^5$ m^2/m^3). This makes the electrochemical reaction zone thinner within the cathode. As a result the current density per active TPB area is lower at the cathode-electrolyte interface (1400 A/m^2 as a maximum value), compared to the anode-electrolyte interface (9400 A/m^2). This gives lower polarizations on the cathode side, but the current density per unity volume is higher on the cathode side ($3.6 \cdot 10^9$ A/m^3 as a maximum value at the cathode/electrolyte interface), compared to the anode side ($1.5 \cdot 10^9$ A/m^3).

The activation polarizations along the flow direction (x-direction) within the anode and the cathode for the standard case are shown in Figure 6. There can be compared with the ones predicted by our previous model [8] in Figure 7, where the electrochemical reactions as well as the activation and concentration polarization are defined as interface conditions at the electrode/electrolyte interfaces. For both models, the cell voltage is defined to 0.7 V and a similar trend is found, i.e., the total polarization decreases along the flow direction (as the temperature increases) and the activation polarizations dominate, compared to the ohmic and the concentration polarizations. However, in this study, the activation polarization on the anode side is bigger than that on the cathode side, partially due to the different AV_e implemented, as discussed in the previous paragraph. This effect was not included when the electrochemical reactions were defined at the electrode/electrolyte interface in our earlier models [3,6,8]. The activation polarization distributions represent the biggest difference between the models. It should be noted that in the current model, the current density per active area and the activation polarization is highest at the electrode/electrolyte interface and decreases rapidly within the electrodes as the distance to the interface increases. On the other hand, the ohmic polarization for the ion transfer for the, within the electrodes, at positions far from the interface increases. The couplings between the different polarizations are defined in eqns (28)-(29). The variation in the ionic polarization through the electrolytes (y-direction in the model) was neglected in the previous models. This comparison clearly shows that the impact of modeling the detailed charge transfer reactions and polarizations is significant, despite that a few micrometer thin reaction zone appeared in both anode and the cathode.

The mole fraction distributions along the main flow direction for hydrogen, water, methane, carbon monoxide and carbon dioxide at the fuel channel/anode interface are shown in Figure 8, and the ones at the cross-section normal to the flow direction at the outlet are presented in Figure 9. The mole fraction of hydrogen decreases along the flow direction (Figure 8) due to the electrochemical reactions close to the anode/electrolyte interface and increases due to the reforming reactions (MSR+WGSR) within the anode. It should be noted that the WGSR is at equilibrium and is pushed towards the left direction as the electrochemical reactions proceed along the flow direction. Large hydrogen mole fraction gradients can be observed through the anode (Figure 9). Water is generated due to the electrochemical reactions and is consumed in the reforming reactions (MSR+WGSR). The mole fraction distribution for water has a large gradient through the anode, because the water molecules need to be transported back through the porous media from the active electrochemical reaction zone to the locations for the reforming reactions and to the fuel channel (to be transported out of the cell). Carbon monoxide is generated in the MSR and consumed in the WGSR, and its mole fraction gradient through the anode (Figure 9) is small and the lowest mole fraction is found at the TPB in the electrochemically active region. The carbon monoxide mole fraction along the flow direction increases initially (Figure 8). Carbon dioxide is generated in the WGSR and transported back through the anode to the fuel channel, and further flows out of the cell with the exhaust fuel stream. Only a small mole fraction gradient can be seen through the anode (Figure 9). For methane a clear mole fraction gradient can be observed through the anode (Figure 9), and the lowest mole fraction is found at the TPB close to the gas outlet (Figure 8-9). Note that not all the methane is converted to hydrogen and carbon monoxide, because of a relatively intermediate operating temperature (for the standard case) and a high activation energy for the MSR (according to the Klein kinetics). The fuel stream outlet concentration of methane can be decreased by recirculation of part of the fuel gas. However, such an investigation is outside the scope of this study.

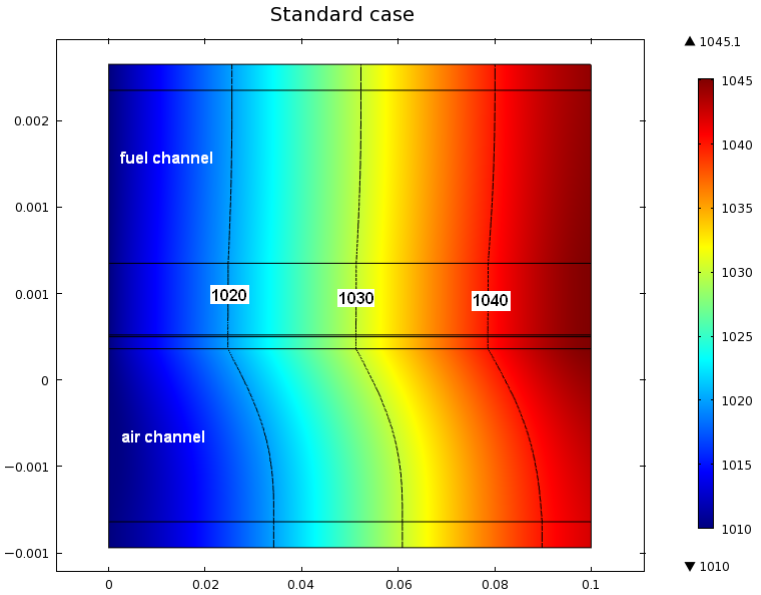

Figure 3. Temperature distribution (K) along the main flow direction of a singe cell.

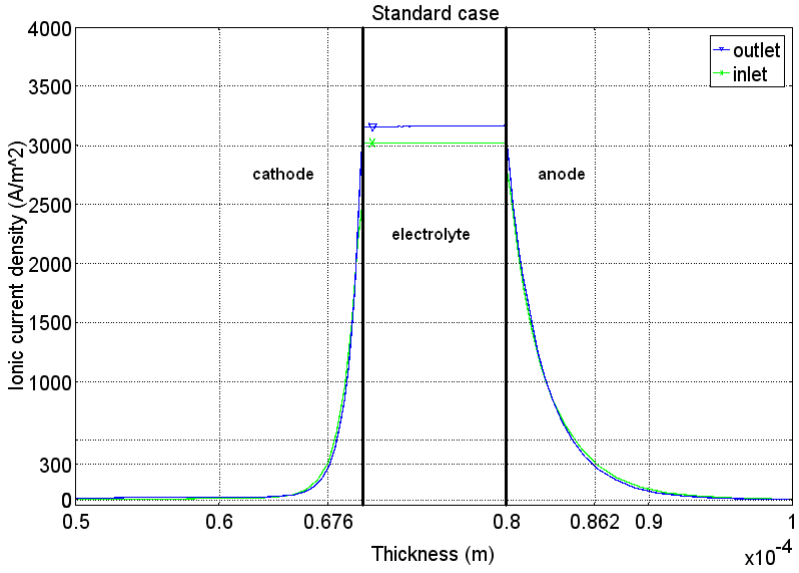

Figure 4. Profile of ion current density (A/m^2). Note that for the anode and cathode, only the parts (20 μm) closest to the electrolyte interface are highlighted in the figure, and the "zero" is assigned at the air channel/cathode interface.

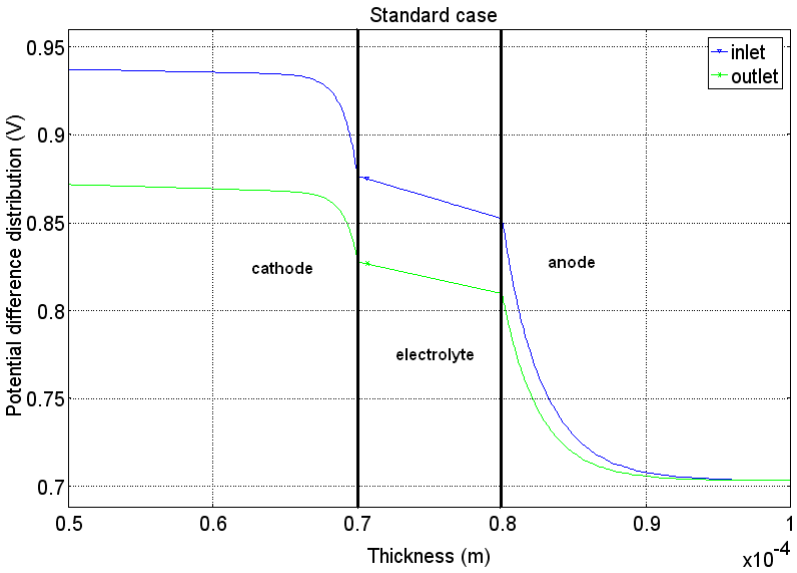

Figure 5. Potential difference distrbution. Note that for the anode and cathode, only the parts (20 μm) closest to the electrolyte interface are shown in the figure, and the "zero" is defined at the air channel/cathode interface.

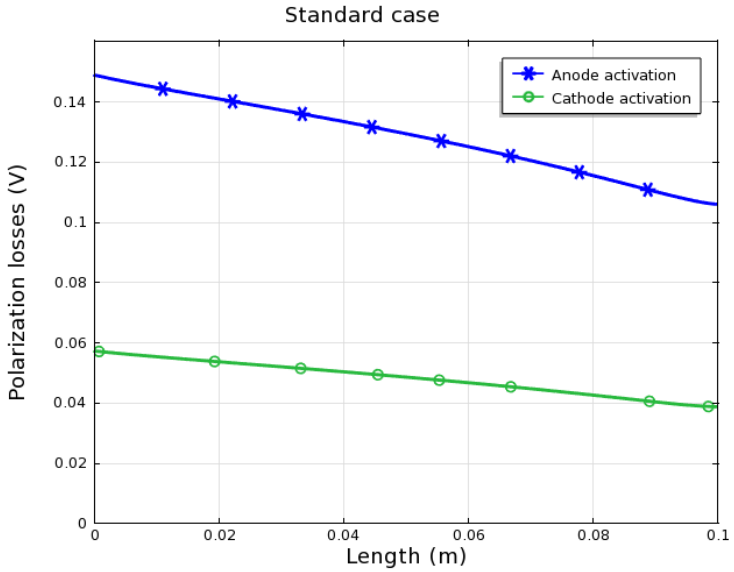

Figure 6. Activation polarization along the flow direction in the andode and cathode predicted by the current model.

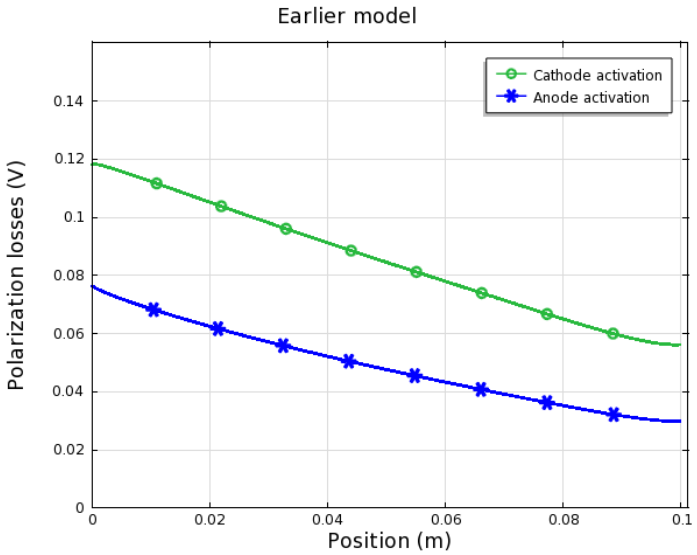

Figure 7. Activation polarization along the flow direction in the anode and cathode predicted by an earlier model [8] (the elctrochemical reactions defined as interface conditions).

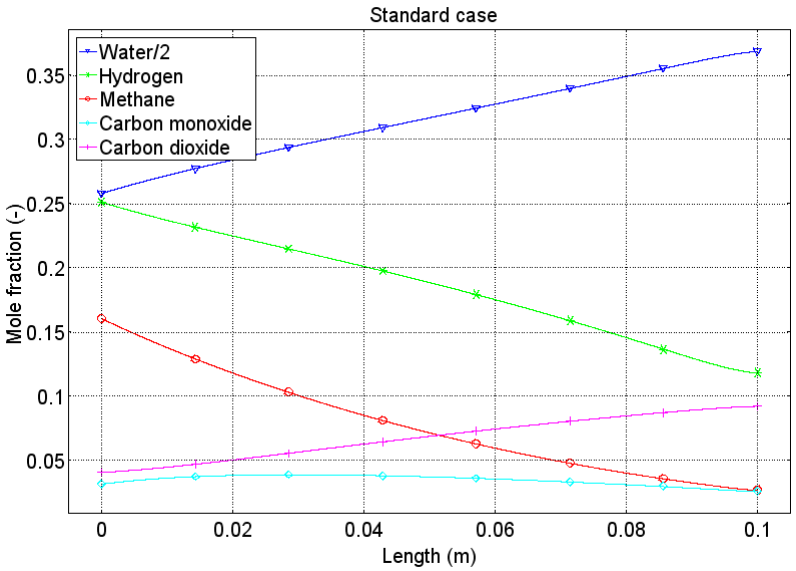

Figure 8. Profiles for mole fractions for water, hydrogen, methane, carbon monoxide and carbon dioxide at the fuel channel/anode interface, along the flow direction. Note that the scales on the y-axis are different and the value should be multiplied with 2 for water.

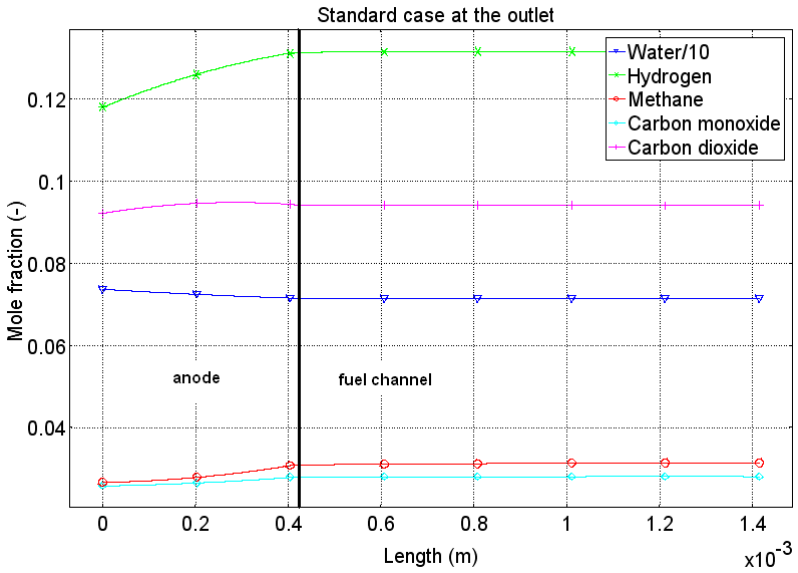

Figure 9. Mole fractions for water, hydrogen, methane, carbon monoxide and carbon dioxide in the anode and fuel channel at the outlet, normal to the flow direction. Note that the scales on the y-axis are different and the value should be multiplied with 10 for water.

As a parameter study, the inlet temperature of the fuel- and air flow streams is increased by 25 K (to 1035 K) to investigate its influence on the cell performance. The fuel- and air flow rates are kept constant, i.e., the fuel- and air utilizations vary, as compared to the standard case above. The temperature distribution for the case with an increased inlet temperature is shown in Figure 10. The difference between the inlet and outlet temperatures is 49 °C, compared to 35 °C for the standard case (Figure 3). An increased inlet temperature means an increased reaction rate, both for the internal steam reforming reactions (i.e., a faster conversion of methane) and for the electrochemical reactions (i.e., a higher current density). Note that the internal reforming reactions consume net heat and the electrochemical reactions generate heat globally. The polarizations decrease due to an increased local temperature. However, the increased current densities also cause an increase of the polarizations.

Figure 11 shows the mole fraction distributions of the gas species at the fuel channel/anode interface along the flow direction. A higher inlet temperature means a higher MSR reaction rate and more methane is converted to hydrogen and carbon monoxide, and consequently a lower methane concentration is found close to the exit. A higher concentration of hydrogen in the inlet region results in a higher ideal voltage and also a higher cell current density. The fuel utilization is around 85 % for this case, compared to 70 % for the standard case (note that the inlet flow rates are kept constant while the cell inlet temperature is increased). The fuel utilizations are evaluated by comparing the fuel gas content at the inlet and at the outlet, where each mole of methane corresponds to 4 moles of hydrogen and each mole of carbon monoxide to 1 mole of hydrogen. The MSR kinetics depend on the activation energy, which is high for the material characteristics in this study, as further discussed in [3,6,25]. An anode catalytic material composition with the low activation energy will result in a higher reaction rate and also a steeper temperature gradient. A disadvantage with an increased temperature gradient is the increased thermal stresses, which can lead to a decreased life time for the operating cell.

The ion current density (in Figure 12) increases as the inlet temperature increases, with a maximum value of around 3950 A/m² at the inlet and 3750 A/m² at the outlet. For the standard case the maximum value is around 3000 A/m² at the inlet and 3200 A/m² at the outlet. The increase in the ion current density is due to the

decreased polarizations and the increased hydrogen concentration, mostly from the MSR by an initially higher hydrogen production. The lower ion current density at the outlet, compared to that at the inlet, is due to a lower concentration of hydrogen at the outlet. The depth of the electrochemically active zones increases slightly to 2.5 µm and 6.3 µm for the cathode and anode, respectively. The corresponding values are 2.4 µm and 6.2 µm for the standard case. It should be noted that the reaction zone is slightly thicker at the inlet compared to the one at the outlet, and the values mentioned here are the averaged ones.

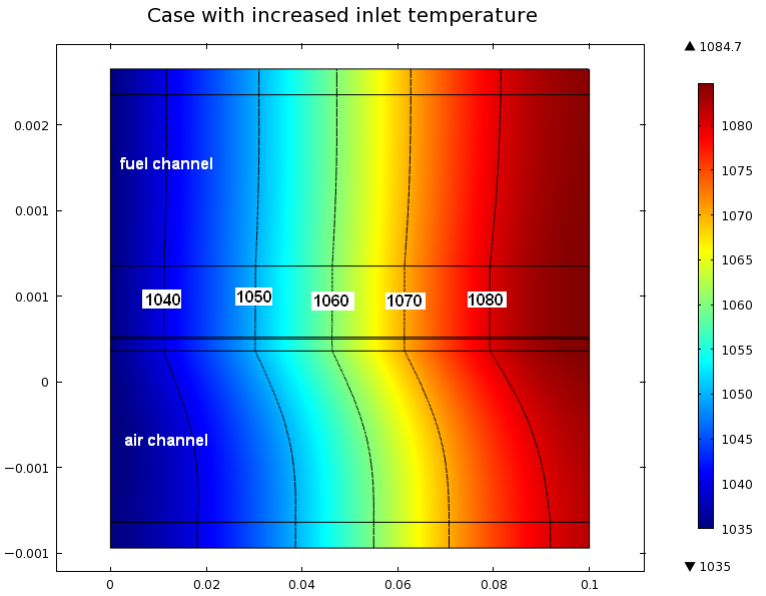

Figure 10. Temperature distribution along the flow direction for the case with increased inlet temperatures (1035 K).

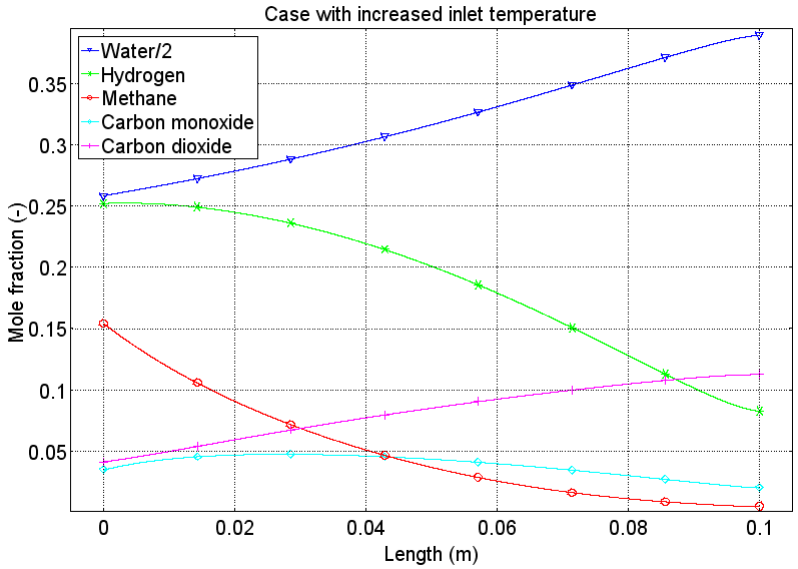

Figure 11. Mole fractions along the flow direction at the fuel channel/anode interface for the case with increased inlet temperatures (1035 K). Note that the scale on the y-axis differs for water, as explained in Figure 8.

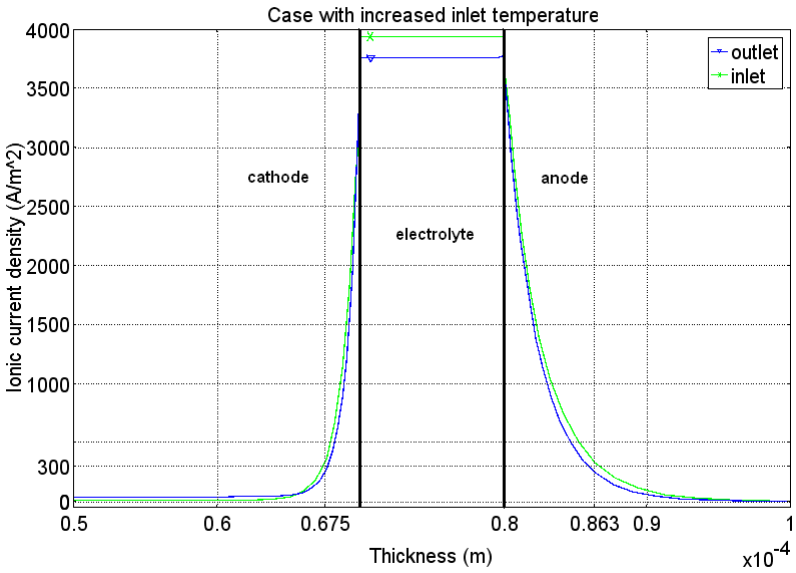

Figure 12. Ion current density (A/m^2) for the case with increased inlet temperatures (1035 K).

Normally the air flow rate is adjusted to make sure that the cell receives sufficient cooling to keep a specific temperature. The air flow rate is, in this study, reduced by 20 % to examine the impact on the temperature distribution (x- and y-directions), the mole fraction variations (x-direction) and the ion current density variations (y-direction). Decreased air flow rates mean decreased cooling and may cause a higher outlet temperature, as shown in Figure 13. The difference between the inlet and outlet temperatures is 50 °C, compared to 35 °C for the standard case in Figure 3. A higher temperature within the cell means a faster consumption of methane and also higher production of carbon monoxide and hydrogen. A higher temperature gradient in the flow direction may decrease the life time for the cell material.

Figure 14 shows the mole fraction distributions of various gas species along the flow direction for the case with a decreased air flow rate. The fuel utilization reaches 75 %, compared to 70 % for the standard case. The increase in fuel utilization is due to a higher methane conversion, despite the outlet concentrations of hydrogen and carbon monoxide are similar to those in the standard case (in Figure 8). The outlet concentration of carbon dioxide is increased compared to the standard case, due to the higher conversion rate of methane. The air utilization is 23 % compared to 18 % for the standard case. The ion current density close to the outlet increases (with a maximum value of around 3600 A/m²), as shown in Figure 15 compared to the standard case (with a maximum value of 3200 A/m²) in Figure 4. This is mainly due to an increased outlet temperature. It should be mentioned that the current density at the inlet is the same as for the standard case. Also the depth of the electrochemically active zones is the same as for the standard case, i.e., 2.4 μm and 6.2 μm for the cathode and anode, respectively.

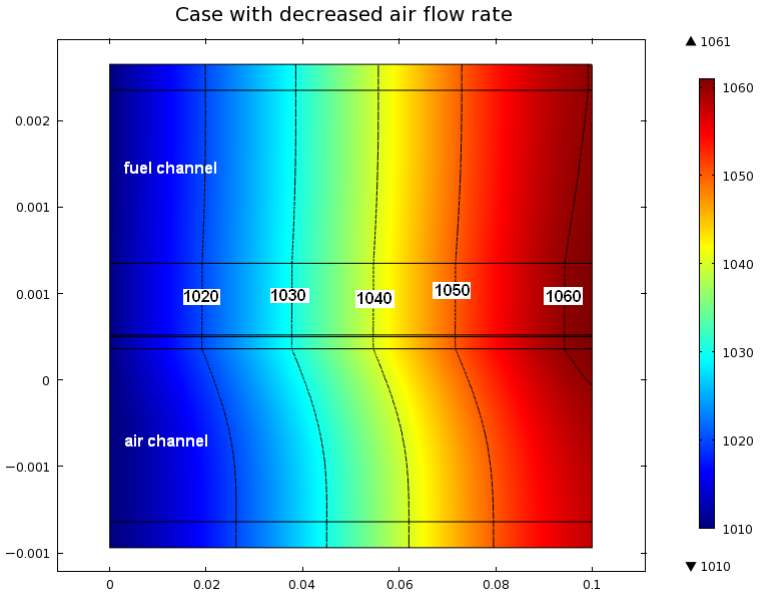

Figure 13. Temperature distribution along the main flow direction for the case with decresed air flow rate.

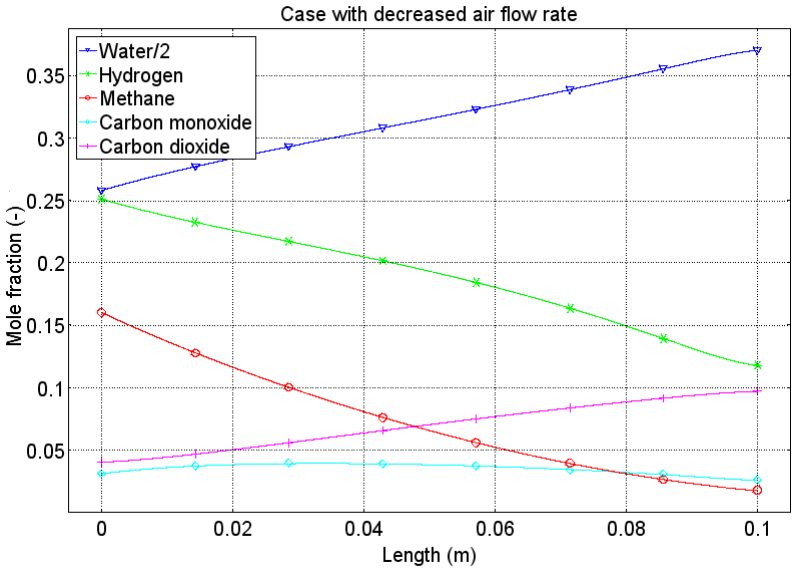

Figure 14. Mole fraction distributions along the flow direction for the case with a decreased air flow rate. Note that the scale on the y-axis for water differs, as explained in Figure 8.

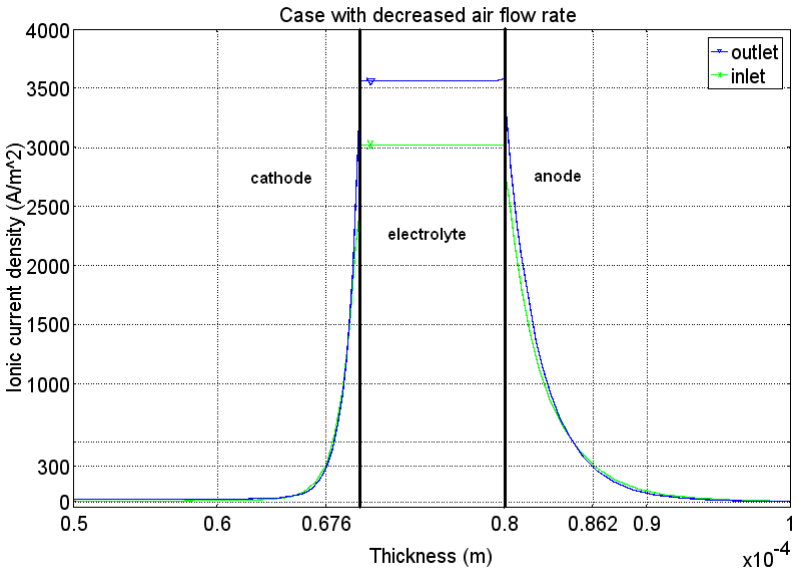

Figure 15. Ion current density (A/m^2) for the case with a decreased air flow rate. Note that the scale for the thickness, (y)-direction, defines "zero" at the air channel/cathode interface.

The ionic tortuosities within the anode and cathode are decreased from 10 for the standard case to 5 to study the influence on the current density and the temperature distributions within the cell. Note that the air- and fuel flow rates are kept constant, i.e., the air- and fuel utilizations are not specified explicitly. The electrochemical reaction zones increase to 3.8 μm on the cathode side and 9.5 μm on the anode side (as shown in Figure 16). For the standard case these are 2.4 μm and 6.2 μm, respectively. Thus the active zone available for the electrochemical reactions increases. A lower ionic tortuosity means a decreased ionic resistance in the electrode. The maximum current density at the inlet is about 4050 A/m², compared to 3000 A/m² for the standard case (Figure 4), and at the outlet 3500 A/m² (compared to 3200 A/m²). The current density at the outlet is lower, than at the inlet, because the fuel utilization increases to 82 % (compared to 70 % for the standard case) and the mole fraction of hydrogen is lower close to the outlet (the minimum value reaches 0.06 compared to 0.12 for the standard case). The outlet temperature is increased due to a higher current density, and it reaches 1052 K (Figure 17) compared to 1045 K for the standard case (Figure 3), even at the same inlet temperature. The temperature gradient close to the inlet is higher as for the standard case, due to large heat generation from the high current density close to the inlet.

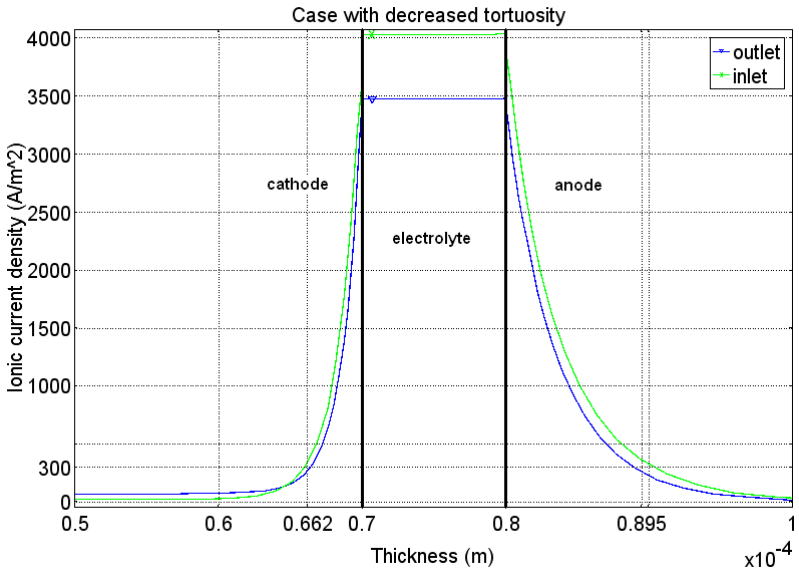

Figure 16. Ion current density (A/m^2) for the case with decreased ionic tortuosity. Note that the scale for the thickness ,(y)-direction, defines "zero" at the air channel/cathode interface.

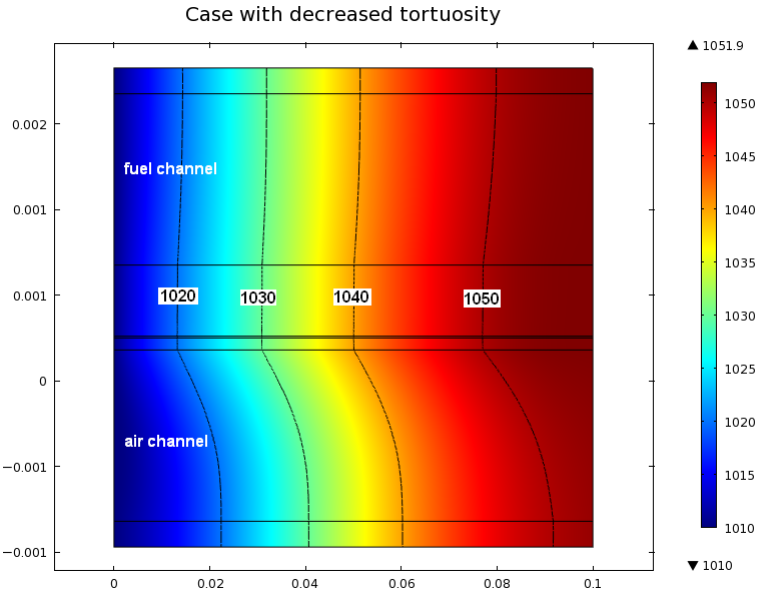

Figure 17. Temperature distribution along the flow direction for the case with decreased ionic tortuosity

5. CONCLUSIONS

A CFD approach is developed and implemented to analyze various chemical and physical phenomena, which take place inside a single cell anode-supported SOFC. Equations for mass-, heat-, momentum-, ion- and electron transport are solved simultaneously and coupling with kinetic expressions for electrochemical and internal steam reforming reactions appearing in various domains is concidered. The model includes correlations for a more realistic description of the transport of the ions and the electrons generated within the anode and the cathode. The ion/electron transport pathways are evaluated by accounting for the volume fractions of the specific materials- and pores, as well as the ionic/electronic tortuosities. The electrochemical reactions are defined in a finite region close to the interface and implemented as various source terms in the relevant governing transport

equations. This is an extension of a previous model, where the electrochemical reactions were defined at indefinitely thin TPBs.

The internal reforming and the electrochemical reaction rates are dependent on the local microscopic structure, temperature and the gas-phase concentrations. The local temperature depends on the reaction rates, the flow rates of the air and fuel streams, the gas-phase concentrations as well as the different polarizations. The gas-phase concentration distribution depends on the temperature, the flow rates of the air and fuel streams as well as the reactions in the electrode porous structure. The ion and electron distributions are affected by the local temperature, the gas-phase concentrations and also the porous material structure. The different polarizations depend on temperature, gas-phase concentrations and porous material structure/design. The above mentioned relationships between the physical parameters/phenomena within a fuel cell show the importance of the couplings between them, i.e., the reason why CFD calculations are necessary and needed to understand the physical phenomena within fuel cells and for improving the fuel cell overall performance, with the overall purpose to reduce the cost and promote commercialization.

Most of the operating parameters are kept constant, while the inlet temperature, air flow rate or the ionic tortuosity are varied for a parameter study. A decreased ionic tortuosity will enable a higher cell current density. In this study the electrons are transported in Ni or LSM and the ions in YSZ. However, other materials are possible for future SOFC designs. This study reveals that the electrochemical reactions occur within only a few micro meters from the electrode/electrolyte interface, e.g., for the standard case 90 % of the electrochemical reactions occur within 2.4 μm in the cathode and 6.2 μm in the anode from the electrode/electrolyte interface. The predicted current density gradient is steeper on the cathode side, compared to the anode side, and it is found that around 60 % of the polarizations occur in the anode, 10 % in the electrolyte and 30 % in the cathode. This conclusion differs from our previous studies, where the electrochemical reactions were implemented as interface conditions in the governing transport equations, and the activation polarization on the cathode side dominated over that on the anode side. This difference can be explained by different current density per (active TPB) area and variable area-to-volume-ratios for the electrochemical reactions within the anode and cathode, respectively. Note that none of these effects are included in our previous models [3,6,8,25]. The current density and the activation polarization are highest at the electrolyte-electrode interface and decreases rapidly within the electrodes as the distance from the interface increases. However, ohmic polarization by ion transfer increases for the positions away from the interface. The current model includes and covers the major transport and reaction phenomena, such as charge transfer, various polarizations, and electrochemical reactions at the TPBs. To increase the knowledge related to these phenomena microscale modeling technique is promising for the future study.

The heat, which is generated within the cell, can be used for the internal steam reforming reaction within the anode and/or outside the cell for external reforming and pre-heating of the fuel and air. The cell current density can be increased by increasing the operating temperature, however, a too high maximum temperature or temperature gradient decreases the cell life time. It is possible to increase the inlet temperature if the air flow rate is also increased, i.e., the maximum temperature is kept constant. As a result, a higher current can be withdrawn from the cell, with a constant voltage. However, some extra energy is needed for the air-pump because the flow rate of air is increased.

NOMENCLATURE

$A_{i,e}$	pre-exponential factor, $1/(\Omega \cdot m^2)$
AV	active area to volume ratio, m^2/m^3
c_p	specific heat at constant pressure, J/(kg·K)
D	diffusion coefficient, m^2/s
D_i^T	thermal diffusion coefficient, kg/(m·s)
E	actual voltage, V
E_a	activation energy, J/mol
E^0	ideal voltage before partial pressure consideration, V
E_{eq}	equilibrium voltage, V
E^{OCV}	ideal voltage after partial pressure consideration, V
F	volume force vector, N/m^3
F	Faraday constant, 96485 C/mol
ΔH	enthalpy change of reaction, J/mol
i	current density, A/m^2
i_0	exchange current density, A/m^2
k	thermal conductivity, W/(m·K)
l_{ij}	characteristic length, Å
M_j	molecular weight of species j, kg/mol, g/mol
n_e	number of electrons transferred per reaction, -
p	pressure, Pa or bar
Q_h	source term (heat), W/m^3
r	reaction rate, $mol/(m^3 \cdot s)$
r_e	pore radius, m
R	gas constant, 8.314 J/(mol·K)
S_i	source term (mass), $kg/(m^3 \cdot s)$
ΔS	entropy change of reaction, J/(K·mol)
T	temperature, K
$\vec{u}$	velocity vector, m/s
V	volume fraction, -
w_i	mass fraction of species i, kg/kg
x, y	coordinate system, m
x_j	mole fraction of species j, mol/mol

Greek symbols

β	transfer coefficient, -
ε	porosity, -
η	over potential (or polarization), V
ϕ	potential, V
κ	permeability, m^2
μ	dynamic viscosity, Pa·s

ρ	density, kg/m^3
σ	ionic/electronic conductivity, $\Omega^{-1}m^{-1}$
τ	tortuosity, -
Ψ	viscous stress tensor, N/m^2
Ω_D	diffusion collision integral, -

Subscripts

a	anode
act	activation
c	cathode
conc	concentration
e	electrode, $e \in \{a, c\}$, electrochemical
el	electrolyte
eff	effective (average)
g	gas-phase
i	(gas-phase) molecule i
j	(gas-phase) molecule j
K	Knudsen diffusion
l	electrolyte material
ohm	ohmic
ref	(internal) reforming reactions
s	solid-phase, electrode material

Abbreviations

CFD	computational fluid dynamics
FC	fuel cell
IEA	International Energy Agency
LTE	local temperature equilibrium
LTNE	local temperature non equlibrium
NIMTE	Ningbo Institute of Material Technology and Engineering
sccm	standard cubic centimeters per minute
SOFC	solid oxide fuel cell
TPB	three-phase boundary

Chemical

CH_4	methane
CO	carbon monoxide
CO_2	carbon dioxide
e^-	elektron
H_2	hydrogen
H_2O	water
LSM	strontium doped lanthanium manganite

Ni	nickel
N_2	nitrogen
O_2	oxygen
YSZ	yttria-stabilized zirconia

ACKNOWLEDGMENTS

The financial support from the Swedish Research Council (VR-621-2010-4581) and the European Research Council (ERC-226238-MMFCs) is gratefully acknowledged. The Chinese Academy of Engineering (CAE) and the Royal Swedish Academy of Engineering Sciences (IVA) have supported the first author for a three month research visit to NIMTE, Chinese Academy of Sciences (CAS) in Ningbo, China.

REFERENCES

[1] J. Staniforth, M. Ormerod, Implications for Using Biogas as a Fuel Source for Solid Oxide Fuel Cells: Internal Dry Reforming in a Small Tubular Solid Oxide Fuel Cell, Catalysis Letter 81 (2002) 19-23.

[2] M. Peksen, R. Peters, L. Blum, D. Stolten, Numerical Modelling and Experimental Validation of a Planar Type Pre-Reformer in SOFC Technology, Int. J. Hydrogen Energy 34 (2009) 6425-6436.

[3] M. Andersson, SOFC Modeling Considering Mass and Heat Transfer, Fluid Flow with Internal Reforming Reactions, Licentiate Thesis, ISRN:LUTMDN/TMHP-09/7063-SE, Department of Energy Sciences, Lund University, Sweden, 2009.

[4] K. Wang, D. Hissel, M.C. Péra, N. Steiner, D. Marra, M. Sorrentino, C. Pianese, M. Monteverde, P. Cardone, J. Saarinen, A Review on Solid Oxide Fuel Cell Models, Int. J. Hydrogen Energy (2011) 7212-7228.

[5] S. Kakac, A. Pramuanjaroenkij, X. Zhou, A Review of Numerical Modeling of Solid Oxide Fuel Cells, I. J. Hydrogen Energy 32 (2007) 761-786.

[6] M. Andersson, J. Yuan, B. Sundén, Review on Modeling Development for Multiscale Chemical Reactions Coupled Transport Phenomena in SOFCs, J. Applied Energy 87 (2010) 1461-1476.

[7] J. Yuan, Y. Huang, B. Sundén, W.G. Wang, Analysis of Parameter Effects on Chemical Coupled Transport Phenomena in SOFC Anodes, Heat Mass Transfer 45 (2009) 471-484.

[8] M. Andersson, J. Yuan, B. Sundén, T.S. Li, W.G. Wang, Modeling Validation and Simulation of an Anode Supported SOFC Including Mass and Heat Transport, Fluid Flow and Chemical Reactions, ESFuelCell2011-54006, in: Proceedings of the ASME 9th International Fuel Cell Science, Engineering & Technology Conference, Washington, DC, USA, 2011.

[9] K. Tseronis, I.K. Kookos, C. Theodoropoulos, Modeling Mass Transport in Solid Oxide Fuel Cell Anodes: A Case for a Multidimensional Dusty Gas-Based Model, Chem. Eng. Sci. 63 (2006) 5626-5638.

[10] J. Shi, X. Xue, CFD Analysis of a Symmetrical Planar SOFC with Heterogeneous Electrode Properties, Electrochimica Acta 55 (2010) 5263-5273.

[11] M. Ni, M.K.H. Leung, D.Y.C. Leung, Micro-Scale Modeling of Solid Oxide Fuel Cells with Micro-Structurally Grades Electrodes, J. Power Sources 168 (2007) 369-378.

[12] Y. Shi, N. Cai, C. Li, Numerical Modeling of an Anode-Supported SOFC Button Cell Considering Anodic Surface Diffusion, J. Power Sources 164 (2007) 639-648.

[13] D. Kanno, N. Shikazono, N. Takagi, K. Matsuzaki, N. Kasagi, Evaluation of SOFC Anode Polarization Simulation Using Three-Dimensional Microstructures Reconstructed by FIB Tomography, Electochimica Acta 56 (2011) 4015-4021.

[14] H. Iwai, N. Shikazono, T. Matsui, H. Teshima, M. Kishimoto, R. Kishida, D. Hayashi, K. Matsuzaki, D. Kanno, M. Saito, H. Muroyama, K. Eguchi, N. Kasagi, H. Yoshida, Quantification of SOFC Anode Microstructure Based on Dual Beam FIM-SEM Technique, J. Power Sources 195 (2010) 955-961.

[15] S.H. Chan, K.A. Khor, Z.T. Xia, A Complete Polarization Model of a Solid Oxide Fuel Cell and its Sensitivity to Change of Cell Component Thickness, J. Power Sources 93 (2001) 130-140.

[16] Y. Patcharavorachot, A. Arpornwichanop, A. Chuachuebsuk, Electrochemical Study of a Planar Solid Oxide Fuel Cell: Role of Support Structures, J. Power Sources 177 (2008) 254-261.

[17] W.G. Bessler, M. Vogler, H. Störmer, D. Gerthsen, A. Utz, A. Weber, E. Ivers-Tiffée, Model Anodes and Anode Models for Understanding the Mechansim of Hydrogen Oxidation in Solid Oxide Fuel Cells, Phys. Chem. Chem. Phys. 12 (2010) 13888-13903.

[18] W.G. Bessler, S. Gewies, M Vogler., A New Framework for Physically Based Modeling of Solid Oxide Fuel Cells, Electrochimica Acta 53 (2007) 1782-1800.

[19] S.A. Hajimolana, M.A. Hussain, W.M.A.W. Daud, M. Soroush, A. Shamiri, Matematical Modeling of Solid Oxide Fuel Cells: A Review, Renewable and Sustainable Energy Reviews 15 (2011) 1893-1917.

[20] D. Mogensen, J.-D. Grunwaldt, P.V. Hendriksen, K. Dam-Johansen, J.U. Nielsen, Internal Steam Reforming in Solid Oxide Fuel Cells: Status and Opportunities of Kinetic Studies and Their Impact on Modelling, J. Power Sources 196 (2011) 25-38.

[21] E. Vakouftsi, G.E. Marnellos, C. Anthansiou, F. Coutelieris, CFD Modelling of a Biogas Fuelled SOFC, Solid State Ionics 192 (2010) 458-463.

[22] F. Nagel, T. Schildhauer, S. Biollaz, S. Stucki, Charge, Mass and Heat Transfer Interactions in Solid Oxide Fuel Cells Operated with Different Fuel Gases – A Sensitivity Analysis, J. Power Sources 184 (2008) 129-142.

[23] P. Aguiar, C.S. Adjiman, N.P. Brandon, Anode-Supported Intermediate Temperature Direct Internal Reforming Solid Oxide Fuel Cell. I: Model-Based Steady-State Performance, J. Power Sources 138 (2004) 120-136.

[24] V. Janardhanan, O. Deutschmann, CFD Analysis of a Solid Oxide Fuel Cell with Internal Reforming: Coupled Interactions of Transport, Heterogeneous Catalysis and Electrochemical Processes, J. Power Sources 162 (2006) 1192-1202.

[25] M. Andersson, H. Paradis, J. Yuan, B. Sundén, Modeling Analysis of Different Renewable Fuels in an Anode Supported SOFC, J. Fuel Cell Science and Technology 8 (2011) 031013.

[26] B. Todd, J.B. Young, Thermodynamic and Transport Properties of Gases for Use in Solid Oxide Fuel Cell Modeling, J. Power Sources 110 (2002)186-200.

[27] W.G. Bessler, J. Warnatz, D.G. Goodwin, The Influence of Equilibrium Potential on the Hydrogen Oxidation Kinetics of SOFC Anodes, Solid State Ionics 177 (2007) 3371-3383.

[28] D.Y. Murzin, T. Salmi, Catalytic Kinetics, Elsevier Science, the Netherlands, 2005.

[29] R.C. Reid, J.M. Prausnitz, B.E. Poling, The Properties of Gases & Liquids, Fourth edition, R.R. Donnelley & Sons Company, USA, 1986.

[30] COMSOL Multiphysics 4.1 user guide, Stockholm, Sweden, 2010.

[31] J.R. Ferguson, J.M. Fiard, R. Herbin, Three Dimensional Numerical Simulation for Various Geometries of Solid Oxide Fuel Cells, J. Power Sources 58 (1996) 109-122.

[32] N. Vivet, S. Chupin, E. Estrade, T. Piquero, P.L. Pommier, D. Rochais, E. Bruneton, 3D Microstructure Characterization of a Solid Oxide Fuel Cell Anode Reconstructed by Focused Ion Beam Tomography, J. Power Sources 196 (2011) 7541-7549.

[33] Fuel Cell Handbook (7^{th} edition), United States Department of Energy, Morgantown, West Virginia, USA, 2004.

[34] M. Kemm, Dynamic Solid Oxide Fuel Cell Modelling for Non-steady State Simulation of System Applications, Doctoral thesis, ISBN:91-628-6981-7, Department of Energy Sciences, Lund University, Sweden, 2006

[35] W. Winkler, P. Nehter, Thermodynamics of Fuel Cells, Fuel Cells and Hydrogen Energy 1 (2008) 15-50.

[36] P. Hofmann, K.D. Panopoulos, L.E. Fryda, E. Kakaras, Comparison between Two Methane Reforming Models Applied to a Quasi-Two-Dimensional Planar Solid Oxide Fuel Cell Model, Energy 34 (2008) 2151-2157.

[37] N. Akhtar, S.P. Decent, K. Kendall, Numerical Modelling of Methane-Powered Micro-Tubular, Single-Chamber Solid Oxide Fuel Cell, J. Power Sources 195 (2010) 7796-7807.

[38] Y. Shi, N. Cai, C. Li, C. Bao, E. Croiset, J. Qian, Q. Hu, S. Wang, Modeling of an Anode-Supported Ni-YSZ|Ni-ScSZ|ScSZ|LSM-ScSZ Multiple Layers SOFC Cell Part I. Experiments, Model Development and Validation, J. Power Sources 172 (2007) 235-245.

[39] A.V. Akkaya, Electrochemical Model for Performance Analysis of a Tubular SOFC, Int. J. Energy Research 31 (2007) 79-98.

[40] A. Konno, H. Iwai, K. Inuyama, A. Kuroyanagi, M. Saito, H. Yoshida, K. Kodani, K. Yoshikata, Mesoscale-Structure Control at Anode/Electrolyte Interface in Solid Oxide Fuel Cell, J. Power Sources 196 (2011) 98-109.

[41] S. Sohn, J.H. Nam, D.H. Jeon, C.J. Kim, A Micro/Macroscale Model for Intermediate Temperature Solid Oxide Fuel Cells with Prescribed Fully-Developed Axial Velocity Profile in Gas Channels, Int. J. Hydrogen Energy 35 (2010) 11890-11907.

[42] Xiao H., Reitz T.L., M.A. Rottmayer., Polarization Measurements of Anode-Supported Solid Oxide Fuel Cells Studied by Incorporation of a Reference Electrode, J. Power Sources183 (2008) 46-54.

[43] J.-M. Klein, Y. Bultel, S. Georges, M. Pons, Modeling of a SOFC Fuelled by Methane: From Direct Internal Reforming to Gradual Internal Reforming, Chem. Eng. Sci. 62 (2007) 1636-1649.

[44] B.A. Haberman, J.B. Young, Three-Dimensional Simulation of Chemically Reacting Gas Flows in the Porous Support Structure of an Integrated-Plannar Solid Oxide Fuel Cell, Int. J. Heat and Mass Transfer 47 (2004) 3617-3629.

[45] V.A. Danilov, M.O. Tade, A CFD-Based Model of a Planar SOFC for Anode Flow Field Design, Int. J. Hydrogen Energy 34 (2009) 8998-9006.

[46] S.T. Aruna, M. Muthuraman, K.C. Patil, Synthesis and Properties of Ni-YSZ Cermet: Anode Materials for Solid Oxide Fuel Cells, Solid State Ionics 111 (1998) 45-51.

[47] M. Mamak, N. Coombs, G.A. Ozin, Practical Solid Oxide Fuel Cells with Anodes derived From Self-Assembeled Mesoporous-NiO-YSZ, Chem. Commun. 20 (2002) 2300-2301.